

Pt(II) Metal Complexes Tailored with a Newly Designed Spiro-Arranged Tetradentate Ligand; Harnessing of Charge-Transfer Phosphorescence and Fabrication of Sky Blue and White OLEDs

Kuan-Yu Liao,[†] Che-Wei Hsu,[†] Yun Chi,^{*,†} Ming-Kuan Hsu,[‡] Szu-Wei Wu,[‡] Chih-Hao Chang,^{*,‡} Shih-Hung Liu,[§] Gene-Hsiang Lee,[§] Pi-Tai Chou,^{*,§} Yue Hu,^{||} and Neil Robertson^{*,||}

[†]Department of Chemistry, National Tsing Hua University, Hsinchu 30013, Taiwan

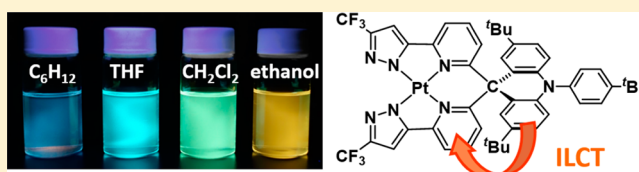
[‡]Department of Photonics Engineering, Yuan Ze University, Chungli 32003, Taiwan

[§]Department of Chemistry, National Taiwan University, Taipei 10617, Taiwan

^{||}EaStCHEM, School of Chemistry, University of Edinburgh, King's Buildings, West Mains Road, Edinburgh EH9 3 FJ, U.K.

S Supporting Information

ABSTRACT: Tetradentate bis(pyridyl azolate) chelates are assembled by connecting two bidentate 3-trifluoromethyl-5-(2-pyridyl)azoles at the six position of pyridyl fragment with the tailored spiro-arranged fluorene and/or acridine functionalities. These new chelates were then utilized in synthesizing a series of Pt(II) metal complexes [Pt(L_n)], *n* = 1–5, from respective chelates L1–L5 and [PtCl₂(DMSO)₂] in 1,2-dimethoxyethane. The single-crystal X-ray structural analyses were executed on 1, 3, and 5 to reveal the generalized structures and packing arrangement in crystal lattices. Their photophysical properties were measured in both solution and solid state and are discussed in the context of computational analysis. These L1–L5 coordinated Pt(II) species exhibit intense emission, among which complex 5 shows remarkable solvatochromic phosphorescence due to the dominant intraligand charge transfer transition induced by the new bis(pyridyl azolate) chelates. Moreover, because of the higher-lying highest occupied molecular orbital of acridine, complex 5 can be considered as a novel bipolar phosphor. Successful fabrication of blue and white organic light-emitting diodes (OLEDs) using Pt(II) complexes 3 and 5 as the phosphorescent dopants are reported. In particular, blue OLEDs with 5 demonstrated peak efficiencies of 15.3% (36.3 cd/A, 38.0 lm/W), and CIE values of (0.190, 0.342) in a double-emitting layer structure. Furthermore, a red-emitting Os(II) complex and 5 were used to fabricate warm-white OLEDs to achieve peak external quantum efficiency, luminance efficiency, and power efficiency values as high as 12.7%, 22.5 cd/A, and 22.1 lm/W, respectively.



INTRODUCTION

Recently, there has been a great research effort into third-row luminescent metal complexes due to high emission quantum yields and long-lived excited states caused by the efficient, heavy metal atom-induced fast singlet/triplet intersystem crossing.^{1–7} The capability to design and prepare strongly luminescent materials facilitates their applications in organic light emitting devices (OLEDs) as well as other technologies, such as chemical, pressure, and oxygen sensors,^{8–13} all via the enhanced participation of the lowest-energy triplet excited states. As a result, emphasis has been switched from organic fluorescent materials to transition-metal-based phosphors with cyclometalating chelates; the latter include those with the octahedral Os(II) and Ir(III) metal complexes with d⁶-electronic configuration and the square-planar Pt(II) complexes bearing d⁸-configuration. One important characteristic of the Os(II) and Ir(III) metal phosphors is the easily accessible Os(III) and Ir(IV) oxidation states, which render a greater amount of metal-to-ligand charge transfer (MLCT) character upon excitation. On the other hand, the oxidation of Pt(II) to Pt(III) is less preferred, meaning that the MLCT contribution should be less influential versus that of

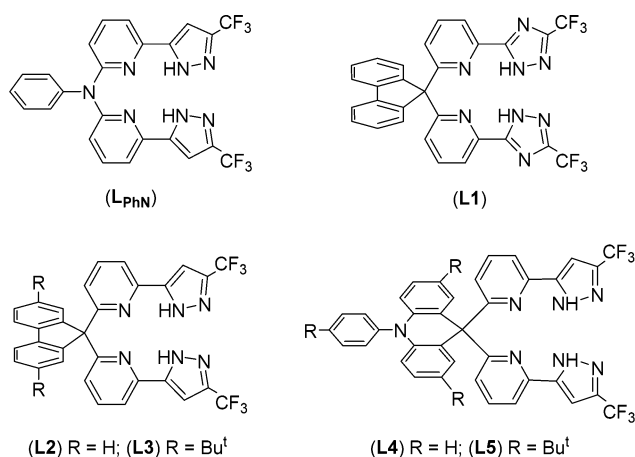
the ligand-centered $\pi\pi^*$ in the lowest-energy excited states. This reduced MLCT character may allow other less-common transition processes, such as intraligand charge transfer (ILCT), to play a dominant role in the lower-lying electronic transition. Similar behavior was documented in the 2-vinylpyridine-type Pt(II) complexes, for which the excited-state characteristics and emission color have been successfully tuned by attachment of different main-group substituents on the chelating cyclometalate.¹⁴

Very recently, we described a new kind of tetradentate chelate (L_{PhN}), which utilizes a single phenylamido appendage to connect the pyridyl unit of two bidentate 2-pyridyl pyrazoles (Chart 1).¹⁵ This design is feasible as it can be assembled using a synthetic protocol similar to those reported for its bidentate counterpart. Moreover, the phenylamido unit provides a flexible skeletal arrangement with the desired tetradentate motif, such that both the reaction intermediate and product may be formed in a stepwise and controllable manner. However, the Pt(II)

Received: February 5, 2015

Published: April 7, 2015

Chart 1. Structural Drawing of Tetradentate Chelates Based on 2-Pyridyl Pyrazole



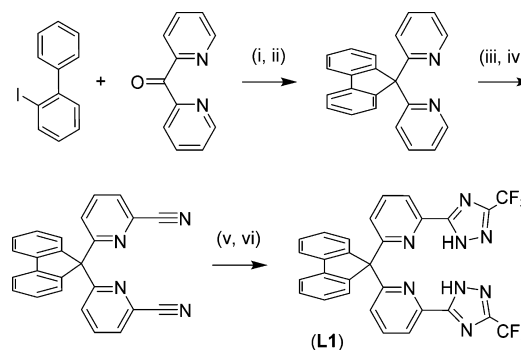
complexes bearing this class of chelates are highly insoluble in common organic solvents, which has hampered the subsequent studies on their basic photophysics and application such as fabrication of OLEDs. Apparently, the phenylimido appendage is incapable of shielding the intermolecular $\pi\pi$ interaction between the square-planar Pt(II) coordination frameworks. This disadvantage makes development of alternative ligand design an urgent task.

Herein, we report the preparation of a new series of tetradentate chelates using spiro-arranged fluorene and acridine linking to the pyrid-2-yl triazole (or pyrazole) units; also see Chart 1. It is thus expected that the perpendicular arranged spiro-fluorene and acridine should provide enough steric hindrance to reduce the intermolecular $\pi\pi$ -stacking interaction between this class of square-planar Pt(II) complexes, give suitable solubility for the measurement of photophysical data, and, hence, give better processability for the fabrication of OLEDs. Moreover, since acridine is a stronger electron-donating moiety than fluorene,^{16–19} we expected that, under suitable conditions, its electron-rich nature would alter the photophysical properties and convert the transition characteristics from ligand-centered $\pi\pi^*$ state to an ILCT state. Phosphors with such an inherent electron-donating (or hole-transporting) functional group were occasionally referred to as bipolar phosphors.^{20–23} Furthermore, because of the large variation in electric dipolar vector, notable solvatochromism in emission was observed by changing the solvent polarity, achieving an exceedingly broad range of color tunability. Elaborated below are the preparation and the associated studies on the photophysical properties and OLED devices involving this new class of luminescent Pt(II) complexes with tetradentate chelates.

RESULTS AND DISCUSSION

Synthesis and Characterization. All required tetradentate chelates **L1**–**L5** contain either a spiro-fluorene or acridine unit linked to two bidentate pyrid-2-yl triazole (or pyrazole) fragments at the six position of their pyridyl sites. Scheme 1 depicts the schematic synthetic pathways leading to the fluorene-bridged pyrid-2-yl triazole (**L1**). First, the key intermediate, 2,2'-(9-fluorenylidene)dipyridine, was synthesized by a two-step processes involving the combination of di(pyridin-2-yl)methanone and an in situ-generated 2-lithiobiphenyl, followed by dehydration in a mixture of acetic anhydride and hydrochloric acid.²⁴ Subsequent pyridine oxidation using hydrogen peroxide

Scheme 1. Synthetic Procedures for L1^a

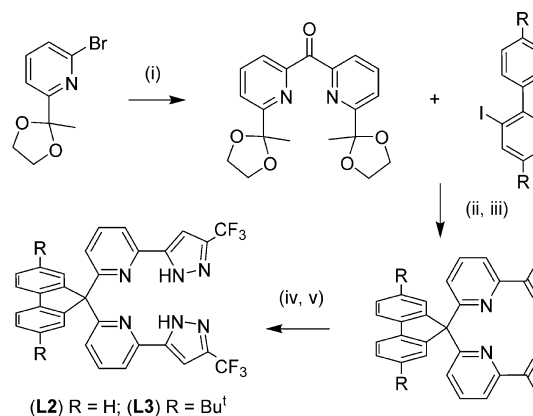


^aExperimental conditions: (i) *n*-BuLi, -78 °C, (ii) (MeCO)₂O, HCl, reflux, (iii) H₂O₂, MeCO₂H, (iv) Me₃SiCN, (v) NH₄Cl, NaOMe, (vi) CF₃CONHNH₂.

in glacial acetic acid and cyanation using Me₃SiCN afforded the 6,6'-(9-fluorenylidene)dipicolinonitrile (Scheme 1).²⁵ Conversion to bitriazole chelate **L1** was then achieved by treatment of the as-synthesized dipicolinonitrile with NH₄Cl in methanol to afford the pyridinecarboximidamide,²⁶ followed by treatment with trifluoroacetic acid hydrazide in a stainless steel digestion bomb.

Scheme 2 shows the preparation procedures to the corresponding fluorene-bridged pyrid-2-yl pyrazole, (**L2**), R =

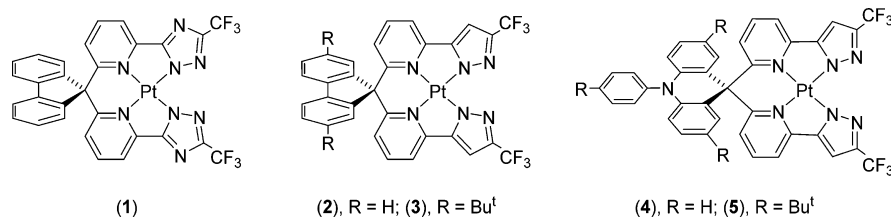
Scheme 2. Synthetic Procedures for L2 and L3^a



^aExperimental conditions: (i) *n*-BuLi, -78 °C, ⁱPrOC(O)Cl, -78 °C–RT, (ii) *n*-BuLi, -78 °C, (iii) (MeCO)₂O, HCl, reflux, (iv) NaH, THF, CF₃CO₂Et, reflux, (v) N₂H₄, EtOH, reflux.

H; (**L3**), R = ^tBu. In this synthetic protocol, we first used 6-bromo-2-(2-methyl-1,3-dioxolan-2-yl)pyridine as the starting material to prepare the key intermediate, bis[3-(2-methyl-1,3-dioxolan-2-yl)pyridin-2-yl]methanone.²⁷ It was then reacted with 2-lithiobiphenyl generated in situ to afford the corresponding coupling products, R = H, ^tBu. Subsequent dehydration and deprotection in acidic media gave formation of both the spiro-fluorene linkage and the acetylpyridine units in a single step. After this, these intermediates can be converted to the desired pyrazole chelates **L2** and **L3** by Claisen condensation with ethyl trifluoroacetate and subsequent cyclization with hydrazine. With these synthetic procedures, the corresponding spiro-acridine chelates, (**L4**), R = H and (**L5**), R = ^tBu, were then synthesized upon employment of acridine precursors, namely, 2-bromo-*N,N*-diphenylaniline and 2-bromo-4-(*t*-butyl)-*N,N*-bis(4-*t*-

Chart 2. Structural Drawing of the Studied Pt(II) Metal Complexes 1–5



butylphenyl)aniline, while keeping all of the synthetic procedures and conditions unaltered.¹⁶ The structural drawings of **L4** and **L5** are depicted in Chart 1 of the introduction section.

The Pt(II) metal complexes **1–5** were then synthesized using respective chelates **L1–L5** and [PtCl₂(DMSO)₂] in 1,2-dimethoxyethane, during which excess of Na₂CO₃ was added to induce deprotonation for optimization of yields. Their structural drawings are depicted in Chart 2. Moreover, it was noted that the *t*-butyl-substituted Pt(II) complexes **3** and **5** showed better solubility in organic solvents versus those without the *t*-butyl substituents (cf. **1**, **2**, and **4**), a result of the lipophilic character of the introduced *t*-butyl substituents.

The X-ray structural analyses of **1**, **3**, and **5** were conducted to disclose their structural arrangement and packing behavior. As indicated in Figures 1–3, the Pt(II) coordination sphere adopts a

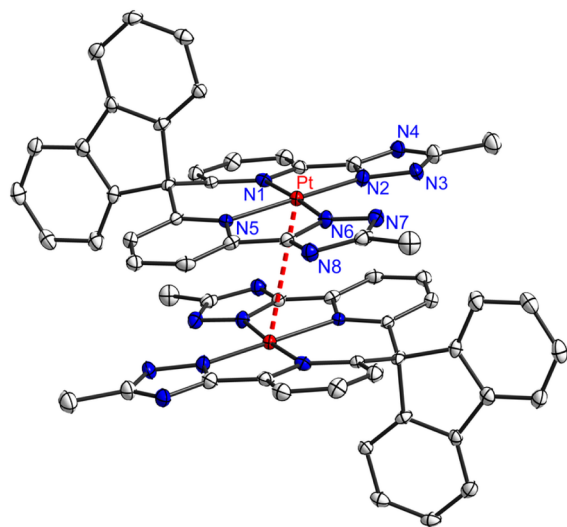


Figure 1. Structural drawing of **1** with thermal ellipsoids shown at 50% probability level, selected bond distances: Pt–N(1) = 2.012(4), Pt–N(2) = 1.975(4), Pt–N(5) = 2.011(4), Pt–N(6) = 1.975(4), and Pt...Pt = 3.759 Å; selected bond angles N(1)–Pt–N(2) = 80.37(15), N(5)–Pt–N(6) = 80.44(15), N(1)–Pt–N(6) = 176.25(15), N(2)–Pt–N(5) = 176.34(15), N(1)–Pt–N(5) = 96.08(14), and N(2)–Pt–N(6) = 103.09(16)°. Fluorine atoms of CF₃ fragments were removed for clarity.

distorted square-planar geometry, for which the average (av) Pt–N_{az} distance to the azolate fragments (1.975(4) Å in **1** vs 1.985(3) Å in **3** and 1.975(5) Å in **5**) is found to be slightly shorter than the av Pt–N_{py} distance to the pyridine fragments (2.012(4) Å in **1** vs 2.017(3) Å in **3** and 2.005(5) Å in **5**). This difference is undoubtedly caused by the anionic character of the triazolate (or pyrazolate) units, for which the Coulomb interaction would be expected to strengthen the associated Pt–N bonding interaction. Moreover, the N_{az}–Pt–N_{az} angle between the azolate fragments (103.09° in **1** vs 95.36° in **3** and 102.1° in **5**) is also larger than the N_{py}–Pt–N_{py} angle between

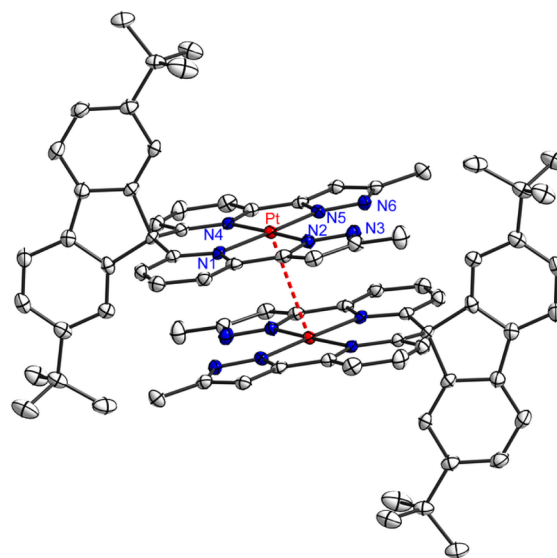


Figure 2. Structural drawing of **3** with thermal ellipsoids shown at 50% probability level, selected bond distances: Pt–N(1) = 2.020(3), Pt–N(2) = 1.980(3), Pt–N(4) = 2.014(3), Pt–N(5) = 1.991(3), and Pt...Pt = 3.455 Å; selected bond angles N(1)–Pt–N(2) = 80.86(13), N(1)–Pt–N(5) = 176.38(13), N(2)–Pt–N(4) = 176.17(13), N(1)–Pt–N(4) = 95.36(13), N(2)–Pt–N(5) = 102.76(13), N(4)–Pt–N(5) = 81.02(13), C(2)–C(1)–C(11) = 123.3(3), and C(20)–C(1)–C(31) = 101.2(3)°. Fluorine atoms of CF₃ fragments were removed for clarity.

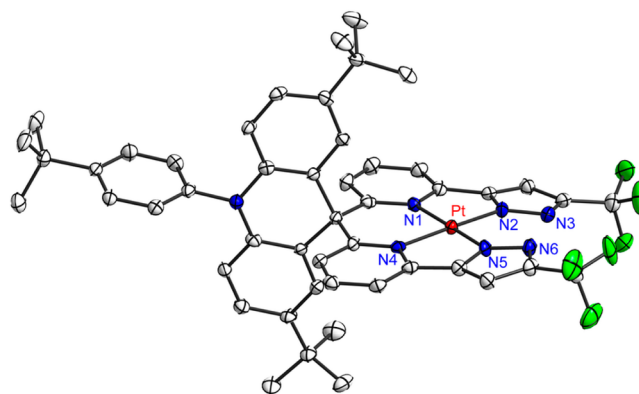


Figure 3. Structural drawing of **5** with thermal ellipsoids shown at 50% probability level, selected bond distances: Pt–N(1) = 2.003(5), Pt–N(2) = 1.982(5), Pt–N(4) = 2.006(5), and Pt–N(5) = 1.967(5) Å; selected bond angles N(1)–Pt–N(2) = 80.69(19), N(4)–Pt–N(5) = 81.03(19), N(1)–Pt–N(5) = 176.79(19), N(2)–Pt–N(4) = 175.61(19), N(1)–Pt–N(4) = 96.24(19), and N(2)–Pt–N(5) = 102.1(2)°.

the pyridyl units (95.36° in **1** vs 80.86° in **3** and 96.24° in **5**), showing the bond-angle expanding effect introduced by either the spiro-fluorene or acridine unit.

Finally, as indicated in their respective packing diagrams, both Pt(II) complexes **1** and **3** exhibited a dimer-like packing motif in the crystal lattice, with the spiro-bridged fluorene unit being tilted away from the second molecule, probably to avoid excessive steric encumbrance. Moreover, the Pt...Pt contact in **3** (3.455 Å) is found to be shorter than that of **1** (3.759 Å), suggesting that the *t*-butyl group fails to exert the anticipated effect of pushing apart the weakly associated dimer. This can be explained by the relative location of the spiro-fluorene unit, as it seems to occupy space further from the cis-coordinated azolate fragments and, hence, exerts almost no steric interference between the pair of dimer molecules. In sharp contrast, the acridine moiety in **5** is much larger than the spiro-fluorene in both **1** and **3**, hence, greatly increasing the spatial separation of the PtN₄ framework between adjacent molecules, allowing the formation of only a monomer in the solid state.

Photophysical Data. The UV-vis absorption and emission spectra of Pt(II) complexes **1–5** in CH₂Cl₂ solution at room temperature (RT) are shown in Figure 4, while the peak wavelengths of absorptions, emissions, and other important photophysical data are summarized in Table 1.

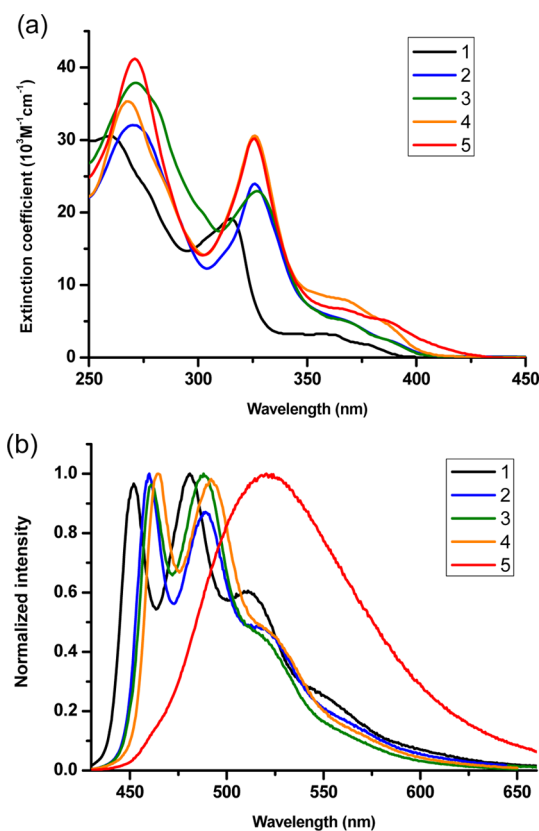


Figure 4. UV-vis absorption and emission spectra of the spiro-arranged Pt(II) metal complexes **1–5** in CH₂Cl₂ at RT. The emission spectra were acquired in the degassed solution. The excitation wavelength for each compound is at the peak position.

As revealed in Figure 4a, obviously the strong absorption bands in the UV region (≤ 330 nm) are derived from a typical ligand-centered $\pi\pi^*$ transition since the corresponding transitions were also documented for the free ligands. As can be seen, the Pt(II) complex **1** displays the most blue-shifted peak wavelength, attributed to the dual triazolite chelates with the enlarged $\pi\pi^*$ energy gap. On the other hand, the other four

Pt(II) complexes with pyrazolate chelates, that is, **2–5**, showed $\pi\pi^*$ absorption at ~ 326 nm, with higher extinction coefficient for the acridine derivatives **4** and **5** due to the greater conjugation versus the fluorene derivatives **2** and **3**.

In addition to the $\pi\pi^*$ absorption, all of these Pt(II) complexes show a weak band at the longer wavelength, which is tentatively assigned to the transition incorporating a mixed state involving both singlet and triplet metal–ligand charge transfer ($^1\text{MLCT}$ and $^3\text{MLCT}$) and, to a certain extent, the ligand-centered $^3\pi\pi$ or $^3\text{ILCT}$ transitions. The absorption onset of these lower-energy bands follows the ascending order of $\mathbf{1} < \mathbf{2} \approx \mathbf{3} < \mathbf{4} \ll \mathbf{5}$ in terms of wavelength, together with a gradual increase in corresponding absorptivity. This trend in spectral shift showed good agreement with the onset of their emission spectra, in which the emission peak maximum (or the E_{00} peak for emission exhibiting vibronic fine structure, see Figure 4b) is in the order of $\mathbf{1}$ (452 nm) $< \mathbf{2}$ (460 nm) $\approx \mathbf{3}$ (461 nm) $< \mathbf{4}$ (465 nm) $\ll \mathbf{5}$ (520 nm, only one peak). As listed in Table 1, the radiative lifetime of >1 μs and quenching of the emission by oxygen (not shown here) demonstrate the phosphorescence origin of the emission.

Remarkably, as shown in Figure 5a, the emission of acridine Pt(II) complex **5** exhibits significant solvatochromism, which is indicated by the observation of a structured emission profile with E_{0-0} of 469 nm in cyclohexane and a broadened structureless emission with a maximum centered between 497–537 nm in the more polar solvents, for example, tetrahydrofuran (THF), CH₂Cl₂, and ethanol. These observations lead us to conclude the occurrence of charge transfer and hence gigantic changes of dipole moment in the excited state versus ground state happen. The quantum yield Φ and lifetime τ were recorded, and the associated radiative (k_r) and nonradiative (k_{nr}) decay rates were deduced from the Φ and τ data using the following equations. These data are listed in Table 2 and can contribute to an in-depth understanding of the solvatochromic effect.

$$(k_r + k_{nr}) = 1/\tau_{\text{obs}} \quad \text{and} \quad \Phi(\%) = k_r/(k_r + k_{nr})$$

As can be seen, a lowered quantum yield $\Phi = 0.13$ and long lifetime $\tau = 20.1$ μs were observed in cyclohexane at RT, which gave the radiative and nonradiative rate constants, k_r of 6.3×10^3 and k_{nr} of 4.3×10^4 . However, increased emission quantum yield $\Phi = 0.88$ and 0.52 and shorter lifetime $\tau = 2.9$ and 2.7 μs were recorded upon switching to more polar solvents such as CH₂Cl₂ and ethanol, from which the substantially increased radiative rate constants k_r of 3.0×10^5 and 1.9×10^5 were deduced. These increased k_r values and disappearance of the vibronic fine structures versus those recorded in cyclohexane can be ascribed, in part, to the involvement of ILCT excited states that effectively harness the triplet emission property. Such a change of emission character from ligand-centered $\pi\pi^*/\text{MLCT}$ to ILCT/MLCT was previously observed in a series of Pt(II) alkynyl complexes with distinctive tridentate pincer ligands, for which the excited-state characters were controlled by the structural design of pincer ligand.²⁸ In sharp contrast, a simple change of solvent polarity seems to be highly effective in causing the associated variation of excited-state character in Pt(II) complex **5**.

The dependence of phosphorescence on solvent polarity can be specified quantitatively according to the dielectric polarization theory. The shift of emission upon increasing solvent polarity depends on the differences in the static dipole moments between the ground (S_0) and (T_1) excited states. The difference of the S_0-T_1 dipole moment can be estimated by the Lippert–Mataga equation incorporating the luminescence solvatochromic shift.²⁹ Considering that the dipole moment of the solute can be

Table 1. Photophysical Data of the Studied Pt(II) Complexes

	abs ^a λ _{max} in nm (ε × 10 ⁻³ M ⁻¹ cm ⁻¹)	em ^a λ _{max} (nm)	Q.Y. (%)	τ _{obs} (μs)	k _r (s ⁻¹)	k _{nr} (s ⁻¹)
1	260 (31), 315 (19), 360 (3), 377 (1.7)	452, 481, 511	60	11.5	5.2 × 10 ⁴	3.5 × 10 ⁴
2	270 (32), 326 (23.9), 368 (5.1), 391 (2.0)	460, 488, 521	67	9.3	7.2 × 10 ⁴	3.5 × 10 ⁴
3	271 (31.8), 327 (22.8), 370 (4.8), 390 (2)	461, 487, 521	82	7.8	1.1 × 10 ⁵	2.3 × 10 ⁴
4	267(35), 325 (30.2), 368 (8), 388 (4.2)	465, 492, 527	58	6.3	9.2 × 10 ⁴	6.7 × 10 ⁴
5	270 (41), 326 (30.5), 367 (6.8), 385 (5.3)	520	88	2.9	3.0 × 10 ⁵	4.2 × 10 ⁴

^aRecorded in CH₂Cl₂ at RT.

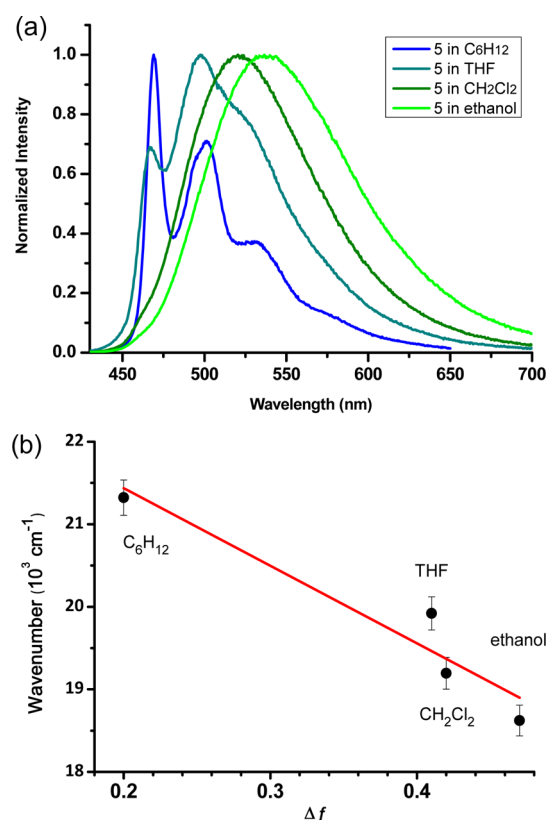


Figure 5. (a) Emission spectra of spiro-acridine Pt(II) complex 5 in various degassed solvents at RT. (b) The Lippert–Mataga plot of phosphorescence as a function of solvent polarity Δf .

Table 2. Photophysical Data of spiro-Acridine Pt(II) Complex 5 in Various Solvents

	em ^a λ _{max} (nm)	Φ (%)	τ _{obs} (μs)	k _r (s ⁻¹)	k _{nr} (s ⁻¹)
cyclohexane	469	13	20.1	6.3 × 10 ³	4.3 × 10 ⁴
THF	497	64	11.8	5.4 × 10 ⁴	3.1 × 10 ⁴
CH ₂ Cl ₂	520	88	2.9	3.0 × 10 ⁵	4.2 × 10 ⁴
ethanol	537	52	2.7	1.9 × 10 ⁵	1.8 × 10 ⁵

^aRecorded at RT.

approximated by a point dipole in the center of a spherical cavity of radius a_0 , on the basis of small solvent-dependent absorption and negligible solute polarizability, one can thus use eq 1 expressed below to describe the emission solvatochromism.

$$\tilde{\nu}_f = \tilde{\nu}_f^{\text{vac}} - \frac{2(\vec{\mu}_e - \vec{\mu}_g)^2}{hca_0^3} \Delta f \quad (1)$$

where $\tilde{\nu}_f$ and $\tilde{\nu}_f^{\text{vac}}$ are the spectral position of the steady-state phosphorescence (in cm⁻¹) and the value extrapolated to the

diluted gas phase, respectively. The $\vec{\mu}_g$ and $\vec{\mu}_e$ are the dipole moment vectors of the ground and T₁ excited states, and Δf is the solvent polarity parameter expressed as $\Delta f = ((\epsilon - 1)/(2\epsilon + 1))$, where ϵ stands for the static dielectric constant of the solvent.

The Lippert plot of the phosphorescence as a function of Δf for Pt(II) complex 5 is shown in Figure 5b. As predicted by eq 1, a linear relationship is found from cyclohexane to ethanol, and slope is deduced to be as steep as -9395 cm^{-1} . The a_0 in eq 1 was estimated to be 9.73 Å by the density functional theory (DFT) Hartree–Fock method (see Experimental Section). Consequently, the change of dipole moment between S₀ and T₁ was calculated to be as large as 29.33 D, firmly supporting the charge transfer character in the T₁ state of 5. Similar solvent-dependent phosphorescence has been reported in the literature,^{30,31} which normally requires the orthogonal orientation and large separation in distance between donor and acceptor ligands to enhance significant changes of dipole moment. For transition metal complexes, the phosphorescence solvatochromism may be observable in the case of either ILCT or ligand-to-ligand charge transfer (LLCT) transition but is much less significant in the case of ligand-centered $\pi\pi^*$ transition.^{2,32}

To gain further fundamental insight into the above experimentally observed absorption and emission spectra, we performed time-dependent density functional theory (TD-DFT) calculations (see Experimental Section). For the Pt(II) complexes 1–5, the frontier molecular orbitals (i.e., highest occupied molecular orbital (HOMO) and lowest unoccupied molecular orbital (LUMO)) involved in the lowest singlet and triplet optical transitions are displayed in Table 3 and Figure 6 (HOMO–1, HOMO, and LUMO). The calculated lowest-lying transition in terms of wavelengths and the charge characters of

Table 3. Calculated Energy Levels and Orbital Transition Analyses of Pt(II) Complexes 1–5

	state	λ (nm)	f	assignments	MLCT
1	S ₁	371.3	0.0019	HOMO → LUMO (96%)	–3.47%
	T ₁	428.3	0	HOMO–1 → LUMO (73%)	16.29%
2	S ₁	370.6	0.0301	HOMO → LUMO (77%)	9.76%
	T ₁	439.3	0	HOMO–1 → LUMO (16%)	7.60%
				HOMO → LUMO (57%)	
				HOMO–1 → LUMO (13%)	
				HOMO–3 → LUMO+1 (7%)	
3	S ₁	375.6	0.0006	HOMO → LUMO (96%)	–4.53%
	T ₁	438.9	0	HOMO–1 → LUMO (70%)	11.50%
				HOMO–3 → LUMO+1 (6%)	
4	S ₁	430.2	0.0001	HOMO → LUMO (99%)	–5.59%
	T ₁	441.2	0	HOMO–1 → LUMO (66%)	10.04%
				HOMO–2 → LUMO+2 (11%)	
				HOMO–2 → LUMO+1 (6%)	
5	S ₁	458.1	0.0002	HOMO → LUMO (100%)	–5.61%
	T ₁	459.5	0	HOMO → LUMO (98%)	–5.50%

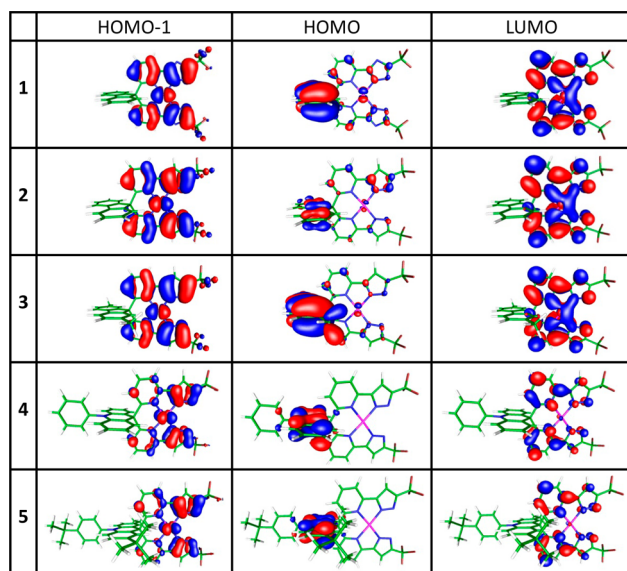


Figure 6. Frontier molecular orbitals (HOMO–1, HOMO, and LUMO) in the lowest-energy optical transitions for Pt(II) complexes 1–5.

the five lowest singlet and triplet optical transitions as well as the corresponding molecular orbitals are listed in Table 3 and Supporting Information, Tables S1–S5 and Figures S1–S5, respectively.

The calculated wavelengths of the $S_0 \rightarrow S_1$ transitions for 1: 371.3 nm, 2: 370.6 nm, 3: 375.6 nm, 4: 430.2 nm, and 5: 458.1 nm (in CH_2Cl_2) are close to the observed onsets of each corresponding absorption spectrum (in CH_2Cl_2 , see Figure 4 and Table 3). Moreover, the calculated wavelengths of the $S_0 \rightarrow T_1$ transitions for 1: 428.3 nm, 2: 439.3 nm, 3: 438.9 nm, 4: 441.2 nm, and 5: 459.5 nm also correlate well to the emission band in Figure 4. The electron density distributions of the key frontier molecular orbitals for Pt(II) complex 1 are mainly localized at the triazolate chelate (for HOMO–1 and LUMO) and fluorene fragment (for HOMO). Similarly, the electron density distributions for Pt(II) complexes 2–5 are mainly located at the pyrazolate chelate and fluorene/acridine (for HOMO–1 and HOMO) and at the pyrazolate chelate (for LUMO). The $S_0 \rightarrow S_1$ and $S_0 \rightarrow T_1$ optical transitions for Pt(II) complexes 1–4 are assigned to the HOMO \rightarrow LUMO or HOMO–1 \rightarrow LUMO, and their MLCT character is within the range from –5.59% (S_1 state of 4) to 16.29% (T_1 state of 1). The negative sign indicates that the charge transfer, in part, involves ligand-to-metal charge transfer (LMCT) or ILCT processes. However, for the T_1 state, which is the origin of the phosphorescence, frontier orbital analyses indicate that all Pt(II) complexes 1–4 are dominated by the distinctive ligand-centered $\pi\pi^*$ transition. In sharp contrast, both S_1 and T_1 of complex 5 possess a great portion of charge transfer character from acridine (HOMO) to the pyrazolate chelates, that is, a typical ILCT transition, but in a mutual orthogonal orientation, resulting in a large separation of electron density between two corresponding moieties. The computational results thus firmly support the experimental observation, expecting the large change of dipole moment between T_1 and S_0 states and thus remarkable phosphorescence solvatochromism for 5. Conversely, the phosphorescence of the other complexes (i.e., 1–4) mainly involves ligand-centered $\pi\pi^*$, which is rather insensitive to the solvent polarity.

We made an attempt to further calculate the lowest singlet and triplet emissions for 5 in four solvents, namely, cyclohexane, THF, CH_2Cl_2 , and ethanol (Table 4). The solvent polarity is in

Table 4. Calculated Wavelengths of the Lowest-Energy Singlet and Triplet Absorptions and Emissions (nm) for Pt(II) Complex 5 in Various Solvents

solvent	ϵ^a	$S_0 \rightarrow S_1$	$S_0 \rightarrow T_1$	$T_1 \rightarrow S_0$	$S_1 \rightarrow S_0$
cyclohexane	2.0	440.2	454.2	515.0	502.8
THF	7.4	456.9	458.4	525.3	517.7
CH_2Cl_2	8.9	458.1	459.5	526.8	520.3
ethanol	24.9	463.9	465.2	532.4	526.6

^a ϵ is the dielectric constant.

an increasing order of cyclohexane < THF < CH_2Cl_2 < ethanol. The calculation was performed via executing the geometry optimization in the respective lowest excited state, that is, S_1 or T_1 state, followed by a vertical (Franck–Condon) transition from S_1 (or T_1) to the ground state (S_0). As a result, the calculated $S_1 \rightarrow S_0$ fluorescence and $T_1 \rightarrow S_0$ phosphorescence in cyclohexane, THF, CH_2Cl_2 , and ethanol are (502.8 and 515.0 nm), (517.7 and 525.3 nm), (520.3 and 526.8 nm), and (526.6 and 532.4 nm), respectively. Interestingly, the calculated phosphorescence, in terms of wavelength, is relatively insensitive to the solvent polarity. This result may not be too surprising because of the application of Onsager solvation model,³³ for which the treatment of continuum spherical shape for solvent molecules lacks the anisotropic dipole orientation; thus, the calculated solvatochromism effect is relatively much smaller than that of the experimental observation.

Organic Light-Emitting Diode Device Fabrication. Pt complexes 3 and 5 were used as dopants for the fabrication of blue phosphorescent OLEDs (PhOLEDs) due to their higher emission quantum efficiencies. On the basis of our previous experience in fabrication of true-blue PhOLEDs,^{34–36} we chose a double-layered design with the following architecture: ITO/TAPC (40 nm)/mCP doped with 8 wt % of Pt complex (17 nm)/DPEPO doped with 8 wt % of Pt complex (3 nm)/DPEPO (3 nm)/TmPyPB (50 nm)/LiF (0.8 nm)/Al (150 nm). Figure 7 presents structural drawings of the employed materials and device architecture. The procedure involved dispersing dopants into hosts with opposite transport properties, so that the carrier recombination zone can be enlarged compared with the single emitting layer (EML). Thus, two wide triplet-energy-gap host materials, 3-bis(9-carbazolyl)benzene (mCP) and bis(2-(diphenylphosphino)phenyl)ether oxide (DPEPO), for which the respective triplet energy gaps (E_T) are reported to be 2.9 and 3.0 eV, were applied in this approach.^{37–42} In addition, mCP shows the hole and electron mobilities to be 1.2×10^{-4} and 3.4×10^{-5} $\text{cm}^2/(\text{V s})$, respectively. The former is an order of magnitude higher.^{37–39} Therefore, the electron-transporting DPEPO was used to combine with mCP to form the second EML and the subsequent exciton confining layer. On the other hand, di-[4-(*N,N*-ditolyl-amino)-phenyl]cyclohexane (TAPC) was used as the hole-transport layer, because it possesses a triplet gap of 2.8 eV, a higher hole mobility of 1×10^{-2} $\text{cm}^2/\text{V s}$, and an upper-lying LUMO level capable of blocking the electron injection, while 1,3,5-tri[(3-pyridyl)-phen-3-yl]benzene (TmPyPB) was used as the electron-transport layer due to the higher carrier-transport capability of 1×10^{-3} $\text{cm}^2/\text{V s}$ and large triplet gap (E_T) of 2.78 eV.^{43–46}

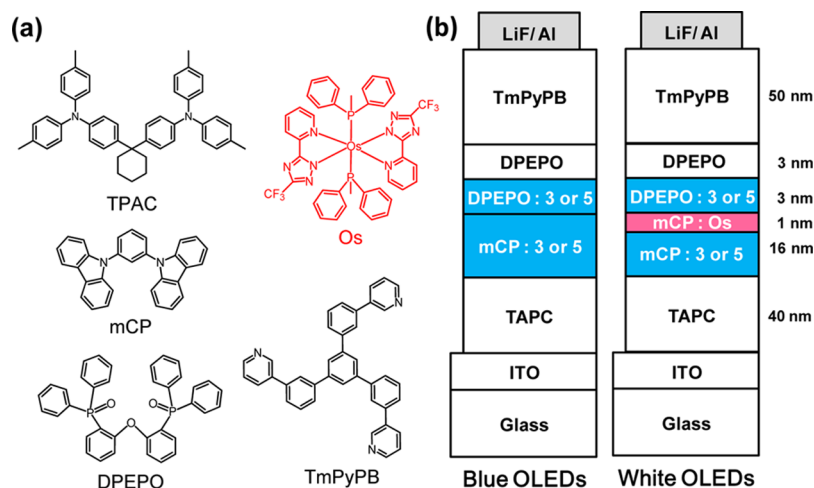


Figure 7. (a) Structural drawing of the materials and (b) schematic structures of the tested blue and white OLEDs.

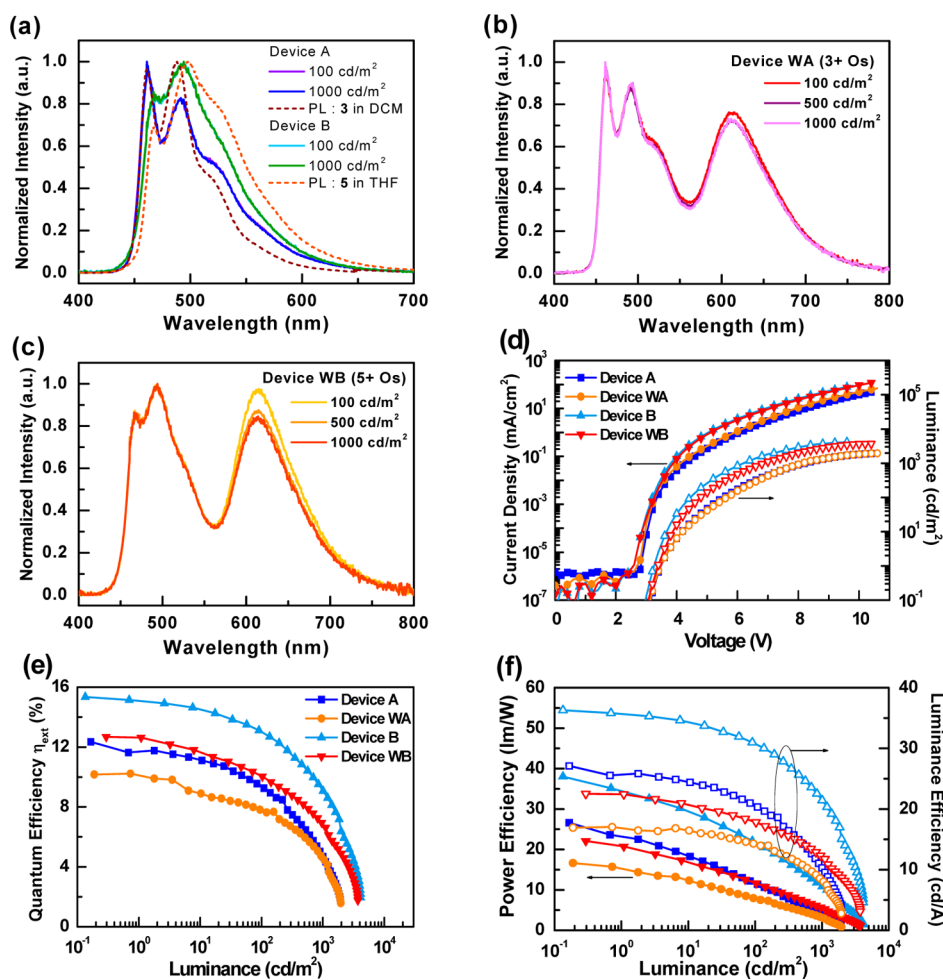


Figure 8. (a) EL spectra of devices A and B, (b) EL spectra of device WA at different luminance levels, (c) EL spectra of device WB at different luminance levels, (d) current density–voltage–luminance (J – V – L) characteristics, (e) external quantum efficiency vs luminance, (f) power efficiencies/luminance efficiencies vs luminance for devices A, B, WA, and WB.

Figure 8 and Table 5 show the electroluminescence (EL) characteristics and the associated numerical data for the devices employing 3 and 5. As shown in Figure 8a, devices A and B exhibited solely the emission of 3 and 5. No interfering emission from either hosts or carrier-transport materials was observed, implying the occurrence of effective exothermic energy transfer

to the dopant. Their EL spectra exhibited stable emission at different luminance, indicating that the exciton formation zones shift insignificantly with increasing voltages. This reduced susceptibility to environmental influence is remarkable. The slightly wider full width at half-maximum (fwhm) of the EL spectra versus that of the photoluminescence (PL) spectra results

Table 5. EL Characteristics of Tested Devices with Different Emitters

emission color device	sky blue			white	
	A	B	WA	WB	
dopant	3	5	3 + Os	5 + Os	
external quantum efficiency (%)	<i>a</i>	12.3	15.3	10.1	12.7
	<i>b</i>	9.4	12.8	7.8	10.0
luminescence efficiency (cd/A)	<i>a</i>	27.1	36.3	16.9	22.5
	<i>b</i>	20.6	30.4	14.2	17.8
power efficiency (lm/W)	<i>a</i>	26.6	38.0	16.6	22.1
	<i>b</i>	11.7	21.1	7.9	11.7
V_{on} (V)	<i>c</i>	3.5	3.2	3.5	3.4
max luminance (cd/m ²) [voltage]		1924 [10.4 V]	4121 [9.8 V]	1945 [10.6 V]	3710 [10.4]
CIE1931 coordinates/CCT (K)/CRI (Ra14)	<i>b</i>	(0.190, 0.342)	(0.194, 0.391)	(0.360, 0.366) 4549 K/70.2	(0.382, 0.375) 3900 K/64.2
	<i>d</i>	(0.189, 0.342)	(0.193, 0.390)	(0.355, 0.362) 4695 K/69.2	(0.369, 0.375) 4313 K/65.1
	<i>e</i>	(0.189, 0.342)	(0.193, 0.389)	(0.355, 0.362) 4684 K/68.3	(0.365, 0.376) 4438 K/65.4

^aMaximum efficiency. ^bRecorded at 1×10^2 cd/m². ^cTurn-on voltage measured at 1 cd/m². ^dMeasured at 500 cd/m². ^eMeasured at 1000 cd/m².

from concentration-induced red-shift as well as the effect of optical interference. Overall, both devices A and B showed sky-blue emission colors and similar CIE coordinates of (0.190, 0.342) and (0.194, 0.391), respectively.

According to the J - V - L curves shown in Figure 8d, device B exhibits a higher current density than device A (8.1 vs 25.9 mA/cm²) at driving voltage of 8 V. The higher current density of 5 indicates better carrier-transport properties, which is also confirmed by the lower turn-on voltage and higher luminance. The corresponding turn-on voltages of A and B obtained at 1 cd/m² were recorded to be 3.5 and 3.2 V, respectively. Moreover, device A gave a maximum luminance of 1924 cd/m² at 10.4 V, while device B achieved a much higher luminance of 4121 cd/m² at a lower driving voltage of 9.8 V. Peak EL efficiencies of up to 12.3%, 27.1 cd/A, and 26.6 lm/W were recorded for A, and the efficiencies remained high at ~9.4%, 20.6 cd/A, and 11.7 lm/W at a practical brightness of 1×10^2 cd/m². Under identical conditions, device B exhibited a maximum efficiency of 15.3%, 36.3 cd/A, and 38.0 lm/W and slightly reduced forward efficiencies of 12.8%, 30.4 cd/A, and 21.1 lm/W at 1×10^2 cd/m². Given the similarity of the PL Φ for both complexes, the better efficiency and the suppressed efficiency roll-off observed in device B was certainly attributed to the superior carrier transport of 5.

Encouraged by the aforementioned performances, we made further attempts to attain white OLEDs (WOLEDs) based on the blue OLED architecture. A red-emitting Os-(fptz)₂(PPh₂Me)₂ can provide a complementary color with respect to the blue emission of 3 and 5 and was thus chosen as the second emitter.⁴⁷ In general, the color variation and carrier balance are significantly influenced by both the location and concentration of red EML layer because of the lower energy gap.^{48–51} To stabilize the resulting emission at different voltages, a thin layer (i.e., 1 nm) of red dopant was sandwiched between the double layers of blue dopant and constituted the principal carrier recombination zone (RZ) in EML.^{52,53} As shown in Figure 8b, the WOLEDs with blue/red/blue EMLs are depicted as follows: ITO (120 nm)/TAPC (40 nm)/mCP doped with 8.0 wt % 3 or 5 (16 nm)/mCP doped with 2.0 wt % Os (1 nm)/DPEPO doped with 8.0 wt % 3 or 5 (3 nm)/DPEPO (3 nm)/TmPyPB (50 nm)/LiF (0.8 nm)/Al (150 nm). Therefore, the low HOMO level of the red dopant will help to localize the RZ, mitigating the color variation induced by the RZ shift as voltage increases.

Figure 8b,c shows the EL spectra at different luminance. Both devices presented stable warm-white emission and a minimized variation of CIE coordinates, that is, (−0.005, −0.004) and (−0.017, 0.001) for devices WA and WB, respectively. The correlated color temperatures (CCT) and color rendering index (CRI) at 100 cd/m² were respectively estimated to be (4549 K, 70) and (3900 K, 64) for WA and WB. The lowered CCTs and CRI values for WB are due to the red-shifted PL emission of 5. As shown in Figure 8d both WOLEDs gave similar current densities, maximum luminescence, and turn-on voltages, respectively. Their maximum efficiencies reached 10.1% (16.9 cd/A, 16.6 lm/W) and 12.7% (22.5 cd/A, 22.1 lm/W) for WA and WB, respectively. In addition, WA exhibited EL efficiencies of 7.8%, 14.2 cd/A, and 7.9 lm/W, while WB exhibited efficiencies of 10.0%, 17.8 cd/A, and 11.7 lm/W, both recorded at 1×10^2 cd/m². These data are summarized in Figure 8e,f.

CONCLUSION

In conclusion, we report the rational design and syntheses of a new series of tetradentate bis(pyridyl azolate) chelates. These chelates offer an orthogonal configuration per se between fluorene and acridine and two bidentate 3-trifluoromethyl-5-(2-pyridyl) azolate chelates that offer four binding sites for the central Pt(II) metal ion. Five Pt(II) metal complexes 1–5 were thus successfully synthesized, for which the Pt(II)–Pt(II) interaction has been minimized due to the intrinsic steric hindrance introduced by the chelates, resulting in the formation of dimeric structure, rather than the one-dimensional chainlike oligomer geometry. These complexes with a well-protected Pt(II) core exhibit intense emission intensity, among which 5 shows remarkable solvatochromism of phosphorescence due to the dominant ILCT transition in orthogonal orientation, as also firmly evidenced by the computational approach. These robust Pt(II) complexes can serve as effective sky blue phosphors for OLEDs. The peak efficiencies of OLEDs with Pt(II) dopants 3 and 5 were recorded at 12.3% (27.1 cd/A, 26.6 lm/W) and 15.3% (36.3 cd/A, 38.0 lm/W), respectively. Furthermore, the red-emitting Os(II) complex, Os(fptz)₂(PPh₂Me)₂, was combined with 3 or 5 to fabricate WOLEDs. Devices WA (i.e., 3 + Os) produced a maximum efficiency of 10.1% and ultrastable warm-white emission with CIE coordinates (0.360, 0.366) at 100 cd/m², while WB (i.e., 5 + Os) achieved even higher peak efficiency of 12.7% and warm-white emission with CIE coordinates (0.382, 0.375) at 100 cd/m². The orthogonality between the auxiliary and intimate coordination framework also offers versatility to

form metal complexes endowed with unique photophysical properties. These outcomes pinpoint the great potential of these series of tetradentate chelates in the coordination chemistry as well as lighting and solar energy research fields.

EXPERIMENTAL SECTION

General Procedures. All solvents were dried over appropriate drying agents and distilled prior to use. Commercially available reagents were used without further purification, unless otherwise stated. All reactions were performed under a nitrogen atmosphere and monitored by using precoated thin-layer chromatography plates (0.20 mm with fluorescent indicator UV254). Mass spectra were obtained on a JEOL SX-102A instrument operating in electron impact (EI) or fast atom bombardment (FAB) mode. All NMR spectra were recorded on a Varian Mercury-400, VNMR-700, or an INOVA-500 instrument. Elemental analysis was performed with a Heraeus CHN-O Rapid Elementary Analyzer.

Synthesis of [Pt(L1)] (1). A mixture of Pt(DMSO)₂Cl₂ (65 mg, 0.15 mmol), Na₂CO₃ (82 mg, 0.77 mmol), and L1 (100 mg, 0.17 mmol) in 1,2-dimethoxyethane (DME) was refluxed for 5 h. After removal of DME, the residue was extracted with CH₂Cl₂, and the CH₂Cl₂ solution was washed with water, dried over Na₂SO₄, and concentrated. The obtained crude product was purified by SiO₂ column chromatography using CH₂Cl₂ and hexane (15:1) as eluent, followed by recrystallization from a mixed solution of CH₂Cl₂ and hexane to obtain a pale yellow solid (62 mg, 51.2%).

Spectral data of 1: ¹H NMR (400 MHz, CD₂Cl₂, 298 K): δ 8.03 (dd, *J* = 7.8, 1.5 Hz, 2 H), 7.98 (d, *J* = 7.5 Hz, 2 H), 7.91 (d, *J* = 7.5 Hz, 2 H), 7.77 (t, *J* = 7.8 Hz, 2 H), 7.58–7.54 (m, 2 H), 7.43–7.40 (m, 2 H), 6.75 (dd, *J* = 8.6, 1.1 Hz, 2 H). ¹⁹F NMR (376 MHz, CDCl₃, 298 K): δ –64.26. MS [FAB], *m/z* 784.1, M⁺. Anal. Calcd for C₂₉H₁₄F₆N₈Pt: C, 44.45; H, 1.80, N, 14.30. Found: C, 45.03; H, 1.92; N, 13.88%.

Selected crystal data of 1: C₃₀H₁₆Cl₂F₆N₈Pt; *M* = 868.50; *T* = 150(2) K; λ(Mo Kα) = 0.710 73 Å; monoclinic; space group = *P*₂₁/*c*; *a* = 9.5855(5), *b* = 25.5533(14), *c* = 11.7334(6) Å, β = 91.4351(13)°; *V* = 2873.1(3) Å³; *Z* = 4; ρ_{calcd} = 2.008 Mg·m⁻³; μ = 5.148 mm⁻¹; *F*(000) = 1672; crystal size = 0.20 × 0.10 × 0.08 mm³; 18 640 reflections collected, 6606 independent reflections (*R*_{int} = 0.0460), max and min transmission = 0.6835 and 0.4258, restraints/parameters = 18/434, GOF = 1.037, final *R*₁[*I* > 2σ(*I*)] = 0.0355, and *wR*₂(all data) = 0.0760.

Synthesis of [Pt(L2)] (2). This complex was prepared from Pt(DMSO)₂Cl₂ and L2 using procedures similar to those described for 1. Yield: 59.8%.

Spectral data of 2: ¹H NMR (400 MHz, acetone-*d*₆, 298 K): δ 8.21 (d, *J* = 7.8 Hz, 2 H), 8.11–8.09 (m, 4 H), 7.94 (t, *J* = 8.4 Hz, 2 H), 7.58 (t, *J* = 7.6 Hz, 2 H), 7.46 (t, *J* = 8.0 Hz, 2 H), 7.42 (s, 2 H), 6.59 (d, *J* = 8.4 Hz, 2 H). ¹⁹F NMR (376 MHz, acetone-*d*₆, 298 K): δ –58.97. MS [FAB], *m/z* 781.0, M⁺. Anal. Calcd for C₃₁H₁₆F₆N₆Pt: C, 47.64; H, 2.06; N, 10.75. Found: C, 48.06; H, 2.39; N, 10.35%.

Synthesis of [Pt(L3)] (3). This complex was prepared from Pt(DMSO)₂Cl₂ and L3 using procedures similar to those described for 1. Yield: 61.2%.

Spectral data of 3: ¹H NMR (400 MHz, CD₂Cl₂, 298 K): δ 7.99 (s, 2 H), 7.79 (d, *J* = 7.6 Hz, 2 H), 7.65 (d, *J* = 4.1 Hz, 4 H), 7.58 (d, *J* = 8.2 Hz, 2 H), 6.99 (s, 2 H), 6.59 (t, *J* = 4.1 Hz, 2 H), 1.26 (s, 18 H). ¹⁹F NMR (376 MHz, CDCl₃, 298 K): δ –61.02. MS [FAB], *m/z* 894.7, M⁺. Anal. Calcd for C₃₉H₃₂F₆N₆Pt: C, 52.41; H, 3.61; N, 9.40. Found: C, 51.96; H, 3.82; N, 9.11%.

Selected crystal data of 3: C₄₀H₃₄Cl₂F₆N₆Pt; *M* = 978.72; *T* = 150(2) K; λ(Mo Kα) = 0.710 73 Å; monoclinic; space group = *P*₂₁/*c*; *a* = 11.2393(5), *b* = 21.0560(11), *c* = 16.0806(8) Å, β = 92.1010(10)°; *V* = 3803.0(3) Å³; *Z* = 4; ρ_{calcd} = 1.709 Mg·m⁻³; μ = 3.898 mm⁻¹; *F*(000) = 1928; crystal size = 0.23 × 0.20 × 0.12 mm³; 24 645 reflections collected, 8737 independent reflections (*R*_{int} = 0.0444), max and min transmission = 0.6520 and 0.4675, restraints/parameters = 0/502, GOF = 1.089, final *R*₁[*I* > 2σ(*I*)] = 0.0366, and *wR*₂(all data) = 0.0791.

Synthesis of [Pt(L4)] (4). This complex was prepared from Pt(DMSO)₂Cl₂ and L4 using procedures similar to those described for 1. Yield: 51.2%.

Spectral data of 4: ¹H NMR (400 MHz, CD₂Cl₂, 298 K): δ 7.87 (t, *J* = 7.9 Hz, 2 H), 7.77 (t, *J* = 7.4 Hz, 2 H), 7.66 (t, *J* = 7.4 Hz, 1 H), 7.60 (d, *J* = 7.9 Hz, 2 H), 7.50–7.47 (m, 2 H), 7.35 (d, *J* = 7.4 Hz, 2 H), 7.17 (dd, *J* = 7.6, 1.7 Hz, 2 H), 7.05–7.00 (m, 4 H), 6.76–6.71 (m, 2 H), 6.42 (d, *J* = 8.4 Hz, 2 H). ¹³C NMR (175 MHz, THF-*d*₈, 298 K): δ 162.7, 152.4, 149.8, 142.2 (q, ²*J*_{C–F} = 35.9 Hz), 140.2, 139.3, 138.0, 131.3, 130.9, 130.8, 128.9, 128.5, 127.7, 125.6, 122.5 (q, ¹*J*_{C–F} = 266.5 Hz), 121.8, 116.9, 115.7, 102.4 (q, ³*J*_{C–F} = 2.2 Hz), 64.4. ¹⁹F NMR (376 MHz, CD₂Cl₂, 298 K): δ –60.96. MS [FAB], *m/z* 871.6, M⁺. Anal. Calcd for C₃₇H₂₁F₆N₇Pt: C, 50.92; H, 2.43; N, 11.24. Found: C, 50.86; H, 2.99; N, 10.85%.

Synthesis of [Pt(L5)] (5). This complex was prepared from Pt(DMSO)₂Cl₂ and L5 using procedures and conditions similar to those described for 1. Yield: 55%.

Spectral data of 5: ¹H NMR (400 MHz, CD₂Cl₂, 298 K): δ 7.85 (t, *J* = 8.5 Hz, 2 H), 7.73 (d, *J* = 6.8 Hz, 2 H), 7.59 (d, *J* = 7.9 Hz, 2 H), 7.33 (d, *J* = 8.5 Hz, 2 H), 7.23 (s, 2 H), 7.05 (d, *J* = 9.1 Hz, 2 H), 7.01 (s, 2 H), 6.36 (d, *J* = 9.1 Hz, 2 H), 1.46 (s, 9 H), 1.01 (s, 18 H). ¹³C NMR (100 MHz, DMSO-*d*₆, 298 K): δ 162.8, 152.3, 150.3, 144.8, 142.8 (q, ²*J*_{C–F} = 36.5 Hz), 139.2, 137.1, 136.3, 130.1, 128.2, 127.7, 126.9, 126.1, 123.9, 122.3 (q, ¹*J*_{C–F} = 266.8 Hz), 117.2, 115.7, 102.6 (q, ³*J*_{C–F} = 2.5 Hz), 65.6, 65.1, 34.8, 33.9, 31.1, 30.8. ¹⁹F NMR (376 MHz, CD₂Cl₂, 298 K): δ –60.99. MS [FAB], *m/z* 1041.3, M⁺. Anal. Calcd for C₄₉H₄₄F₆N₇Pt: C, 56.63; H, 4.36; N, 9.42. Found: C, 56.33; H, 4.52; N, 9.39%.

Selected crystal data of 5: C₅₂H₅₅Cl₂F₆N₇O₂Pt; *M* = 1190.02; *T* = 150(2) K; λ(Mo Kα) = 0.710 73 Å; orthorhombic; space group = *Pbca*; *a* = 14.5851(5), *b* = 25.7640(9), *c* = 26.9502(9) Å; *V* = 10127.1(6) Å³; *Z* = 8; ρ_{calcd} = 1.561 Mg·m⁻³; μ = 2.947 mm⁻¹; *F*(000) = 4784; crystal size = 0.40 × 0.13 × 0.08 mm³; 63 788 reflections collected, 11 632 independent reflections (*R*_{int} = 0.0989), max and min transmission = 0.7984 and 0.3853, restraints/parameters = 7/646, GOF = 1.066, final *R*₁[*I* > 2σ(*I*)] = 0.0504, and *wR*₂(all data) = 0.1295.

X-ray Crystallography. All single-crystal X-ray diffraction data were measured on a Bruker Smart CCD diffractometer using λ (Mo Kα) radiation (λ = 0.710 73 Å). The data collection was executed using the SMART program. Cell refinement and data reduction were made with the SAINT program. The structure was determined using the SHELXTL/PC program and refined using full matrix least-squares. All non-hydrogen atoms were refined anisotropically, whereas hydrogen atoms were placed at the calculated positions and included in the final stage of refinements with fixed parameters.

Organic Light-Emitting Diode Fabrication. All commercial materials and indium tin oxide (ITO)-coated glass were purchased from Nichem and Lumtec. Glass substrates were cleaned by exposure to a UV–ozone atmosphere for 5 min. The bottom-emitting OLED devices were fabricated using ITO-coated glass substrates (<15 Ω) as the anode, followed by the deposition of multiple organic layers, topped by metal cathode layer. The organic and metal layers were consecutively deposited onto the substrates by thermal evaporation in a vacuum chamber with a base pressure of <1 × 10⁻⁶ Torr without breaking the vacuum. The deposition rate was kept at ~0.1 nm/s. The active area of the device was set to 2 × 2 mm², as defined by the shadow mask used for cathode deposition. Current density–voltage–luminance characterization was measured using a Keithley 238 current source-measure unit and a Keithley 6485 picoammeter equipped with a calibrated Si-photodiode. The electroluminescent spectra of the devices were recorded using an Ocean Optics spectrometer.

ASSOCIATED CONTENT

Supporting Information

General experimental procedures, synthesis procedures, NMR and MS data of synthesized compounds, X-ray crystallographic data file (CIF) of Pt(II) complexes 1, 3, and 5, procedures for ligand preparation, illustrated frontier molecular orbitals, absorption and emission spectra, additional references, and results concerning the TD-DFT calculation of all Pt(II) complexes. This material is available free of charge via the Internet at <http://pubs.acs.org>.

AUTHOR INFORMATION

Corresponding Authors

*E-mail: ychi@mx.nthu.edu.tw.

*E-mail: chc@saturn.yzu.edu.tw.

*E-mail: chop@ntu.edu.tw.

*E-mail: Neil.Robertson@ed.ac.uk.

Notes

The authors declare no competing financial interest.

ACKNOWLEDGMENTS

This work was supported by the Ministry of Science and Technology of Taiwan under Grant No. NSC-101-2113-M-007-013-MY3. The computation was conducted at the National Center for High-Performance Computing. Y.H. thanks the China Scholarship Council for a studentship.

REFERENCES

- (1) Chou, P.-T.; Chi, Y. *Eur. J. Inorg. Chem.* **2006**, 3319.
- (2) Chi, Y.; Chou, P.-T. *Chem. Soc. Rev.* **2007**, 36, 1421.
- (3) Williams, J. A. G. *Chem. Soc. Rev.* **2009**, 38, 1783.
- (4) Zhou, G.; Wong, W.-Y.; Yang, X. *Chem.—Asian J.* **2011**, 6, 1706.
- (5) You, Y.; Nam, W. *Chem. Soc. Rev.* **2012**, 41, 7061.
- (6) Chi, Y.; Tong, B.; Chou, P.-T. *Coord. Chem. Rev.* **2014**, 281, 1.
- (7) Pal, A. K.; Hanan, G. S. *Chem. Soc. Rev.* **2014**, 43, 6184.
- (8) Lo, K. K.-W. *Top. Organomet. Chem.* **2010**, 29, 115.
- (9) Zhao, Q.; Li, F.; Huang, C. *Chem. Soc. Rev.* **2010**, 39, 3007.
- (10) Wenger, O. S. *Chem. Rev.* **2013**, 113, 3686.
- (11) Ladouceur, S.; Zysman-Colman, E. *Eur. J. Inorg. Chem.* **2013**, 2013, 2985.
- (12) You, Y.; Cho, S.; Nam, W. *Inorg. Chem.* **2014**, 53, 1804.
- (13) Chang, K.-C.; Sun, S.-S.; Odago, M. O.; Lees, A. J. *Coord. Chem. Rev.* **2015**, 284, 111.
- (14) Yang, X.; Xu, X.; Zhao, J.; Dang, J.-s.; Huang, Z.; Yan, X.; Zhou, G.; Wang, D. *Inorg. Chem.* **2014**, 53, 12986.
- (15) Chang, S.-H.; Chang, C.-F.; Liao, J.-L.; Chi, Y.; Zhou, D.-Y.; Liao, L.-S.; Jiang, T.-Y.; Chou, T.-P.; Li, E. Y.; Lee, G.-H.; Kuo, T.-Y.; Chou, P.-T. *Inorg. Chem.* **2013**, 52, 5867.
- (16) Mehes, G.; Nomura, H.; Zhang, Q.; Nakagawa, T.; Adachi, C. *Angew. Chem., Int. Ed.* **2012**, 51, 11311.
- (17) Chen, H.; Jiang, Z.-Q.; Gao, C.-H.; Xu, M.-F.; Dong, S.-C.; Cui, L.-S.; Ji, S.-J.; Liao, L.-S. *Chem.—Eur. J.* **2013**, 19, 11791.
- (18) Romain, M.; Tondelier, D.; Geffroy, B.; Shirinskaya, A.; Jeannin, O.; Rault-Berthelot, J.; Poriol, C. *Chem. Commun.* **2015**, 51, 1313.
- (19) Liu, T.; Sun, H.; Fan, C.; Ma, D.; Zhong, C.; Yang, C. *Org. Electron.* **2014**, 15, 3568.
- (20) Peng, T.; Li, G.; Ye, K.; Wang, C.; Zhao, S.; Liu, Y.; Hou, Z.; Wang, Y. *J. Mater. Chem. C* **2013**, 1, 2920.
- (21) Tang, M.-C.; Tsang, D. P.-K.; Chan, M. M.-Y.; Wong, K. M.-C.; Yam, V. W.-W. *Angew. Chem., Int. Ed.* **2013**, 52, 446.
- (22) Cheng, G.; Chan, K. T.; To, W.-P.; Che, C.-M. *Adv. Mater.* **2014**, 26, 2540.
- (23) Tang, M.-C.; Tsang, D. P.-K.; Wong, Y.-C.; Chan, M.-Y.; Wong, K. M.-C.; Yam, V. W.-W. *J. Am. Chem. Soc.* **2014**, 136, 17861.
- (24) Wang, C.-C.; Yang, C.-H.; Tseng, S.-M.; Lin, S.-Y.; Wu, T.-Y.; Fuh, M.-R.; Lee, G.-H.; Wong, K.-T.; Chen, R.-T.; Cheng, Y.-M.; Chou, P.-T. *Inorg. Chem.* **2004**, 43, 4781.
- (25) Bell, Z. R.; Motson, G. R.; Jeffery, J. C.; McCleverty, J. A.; Ward, M. D. *Polyhedron* **2001**, 20, 2045.
- (26) Hu, F.-C.; Wang, S.-W.; Planells, M.; Robertson, N.; Padhy, H.; Du, B.-S.; Chi, Y.; Yang, P.-F.; Lin, H.-W.; Lee, G.-H.; Chou, P.-T. *ChemSusChem* **2013**, 6, 1366.
- (27) Barbaro, P.; Bianchini, C.; Giambastiani, G.; Rios, I. G.; Meli, A.; Oberhauser, W.; Segarra, A. M.; Sorace, L.; Toti, A. *Organometallics* **2007**, 26, 4639.
- (28) Lam, W. H.; Lam, E. S.-H.; Yam, V. W.-W. *J. Am. Chem. Soc.* **2013**, 135, 15135.
- (29) Bagchi, B.; Oxtoby, D. W.; Fleming, G. R. *Chem. Phys.* **1984**, 86, 257.
- (30) Yu, J.-K.; Cheng, Y.-M.; Hu, Y.-H.; Chou, P.-T.; Chen, Y.-L.; Lee, S.-W.; Chi, Y. *J. Phys. Chem. B* **2004**, 108, 19908.
- (31) Li, S.-W.; Cheng, Y.-M.; Yeh, Y.-S.; Hsu, C.-C.; Chou, P.-T.; Peng, S.-M.; Lee, G.-H.; Tung, Y.-L.; Wu, P.-C.; Chi, Y.; Wu, F.-I.; Shu, C.-F. *Chem.—Eur. J.* **2005**, 11, 6347.
- (32) Vogler, A.; Kunkely, H. *Coord. Chem. Rev.* **2000**, 208, 321.
- (33) Klamt, A. *J. Phys. Chem.* **1995**, 99, 2224.
- (34) Chiu, Y.-C.; Hung, J.-Y.; Chi, Y.; Chen, C.-C.; Chang, C.-H.; Wu, C.-C.; Cheng, Y.-M.; Yu, Y.-C.; Lee, G.-H.; Chou, P.-T. *Adv. Mater.* **2009**, 21, 2221.
- (35) Chang, C.-H.; Chen, C.-C.; Wu, C.-C.; Yang, C.-H.; Chi, Y. *Org. Electron.* **2009**, 10, 1364.
- (36) Lin, C.-H.; Chang, Y.-Y.; Hung, J.-Y.; Lin, C.-Y.; Chi, Y.; Chung, M.-W.; Lin, C.-L.; Chou, P.-T.; Lee, G.-H.; Chang, C.-H.; Lin, W.-C. *Angew. Chem., Int. Ed.* **2011**, 50, 3182.
- (37) Holmes, R. J.; Forrest, S. R.; Tung, Y.-J.; Kwong, R. C.; Brown, J. J.; Garon, S.; Thompson, M. E. *Appl. Phys. Lett.* **2003**, 82, 2422.
- (38) Eom, S.-H.; Zheng, Y.; Chopra, N.; Lee, J.; So, F.; Xue, J. *Appl. Phys. Lett.* **2008**, 93, 133309.
- (39) Tsuboi, T.; Liu, S.-W.; Wu, M.-F.; Chen, C.-T. *Org. Electron.* **2009**, 10, 1372.
- (40) Han, C.; Zhao, Y.; Xu, H.; Chen, J.; Deng, Z.; Ma, D.; Li, Q.; Yan, P. *Chem.—Eur. J.* **2011**, 17, 5800.
- (41) Lee, S. Y.; Yasuda, T.; Nomura, H.; Adachi, C. *Appl. Phys. Lett.* **2012**, 101, 093306.
- (42) Serevicius, T.; Nakagawa, T.; Kuo, M.-C.; Cheng, S.-H.; Wong, K.-T.; Chang, C.-H.; Kwong, R. C.; Xia, S.; Adachi, C. *Phys. Chem. Chem. Phys.* **2013**, 15, 15850.
- (43) Goushi, K.; Kwong, R.; Brown, J. J.; Sasabe, H.; Adachi, C. *J. Appl. Phys.* **2004**, 95, 7798.
- (44) Zheng, Y.; Eom, S.-H.; Chopra, N.; Lee, J.; So, F.; Xue, J. *Appl. Phys. Lett.* **2008**, 92, 223301.
- (45) Su, S.-J.; Chiba, T.; Takeda, T.; Kido, J. *Adv. Mater.* **2008**, 20, 2125.
- (46) Su, S.-J.; Takahashi, Y.; Chiba, T.; Takeda, T.; Kido, J. *Adv. Funct. Mater.* **2009**, 19, 1260.
- (47) Liu, T.-H.; Hsu, S.-F.; Ho, M.-H.; Liao, C.-H.; Wu, Y.-S.; Chen, C. H.; Tung, Y.-L.; Wu, P.-C.; Chi, Y. *Appl. Phys. Lett.* **2006**, 88, 063508.
- (48) Yook, K. S.; Jeon, S. O.; Joo, C. W.; Lee, J. Y. *Appl. Phys. Lett.* **2008**, 93, 113301.
- (49) Chang, C.-H.; Lin, Y.-H.; Chen, C.-C.; Chang, C.-K.; Wu, C.-C.; Chen, L.-S.; Wu, W.-W.; Chi, Y. *Org. Electron.* **2009**, 10, 1235.
- (50) Chang, C.-H.; Tien, K.-C.; Chen, C.-C.; Lin, M.-S.; Cheng, H.-C.; Liu, S.-H.; Wu, C.-C.; Hung, J.-Y.; Chiu, Y.-C.; Chi, Y. *Org. Electron.* **2010**, 11, 412.
- (51) Chang, C.-H.; Chen, C.-C.; Wu, C.-C.; Chang, S.-Y.; Hung, J.-Y.; Chi, Y. *Org. Electron.* **2010**, 11, 266.
- (52) Su, S.-J.; Gonmori, E.; Sasabe, H.; Kido, J. *Adv. Mater.* **2008**, 20, 4189.
- (53) Chang, C.-H.; Wu, Z.-J.; Chiu, C.-H.; Liang, Y.-H.; Tsai, Y.-S.; Liao, J.-L.; Chi, Y.; Hsieh, H.-Y.; Kuo, T.-Y.; Lee, G.-H.; Pan, H.-A.; Chou, P.-T.; Lin, J.-S.; Tseng, M.-R. *ACS Appl. Mater. Interfaces* **2013**, 5, 7341.